



Institut für Numerische Simulation

Rheinische Friedrich-Wilhelms-Universität Bonn

Friedrich-Hirzebruch-Allee 7 • 53115 Bonn • Germany  
phone +49 228 73-69828 • fax +49 228 73-69847  
[www.ins.uni-bonn.de](http://www.ins.uni-bonn.de)

A. Pakiman, J. Garcke, A. Schumacher

**SimRank-based Prediction  
of Crash Simulation Similarities**

INS Preprint No. 2210

2022



# SimRank-based Prediction of Crash Simulation Similarities

Anahita Pakiman <sup>1,2\*</sup>, Jochen Garcke <sup>1,3</sup> and Axel Schumacher <sup>2</sup>

<sup>1</sup>Fraunhofer SCAI, Sankt Augustin, Germany.

<sup>2</sup>Bergische Universität Wuppertal, Wuppertal, Germany.

<sup>3</sup>Institut für Numerische Simulation, Universität Bonn, Bonn, Germany.

\*Corresponding author(s). E-mail(s): [anahita.pakiman@scai.fraunhofer.de](mailto:anahita.pakiman@scai.fraunhofer.de);  
Contributing authors: [jochen.garcke@scai.fraunhofer.de](mailto:jochen.garcke@scai.fraunhofer.de); [schumacher@uni-wuppertal.de](mailto:schumacher@uni-wuppertal.de);

## Abstract

Data searchability has been utilized for decades and is now a crucial ingredient of data reuse. However, data searchability in industrial engineering is essentially still at the level of individual text documents, while for finite element (FE) simulations no content-based relations between FE simulations exist so far. Additionally, the growth of data warehouses with the increase of computational power leaves companies with a vast amount of engineering data that is rarely reused. Search techniques for FE data, which are in particular aware of the engineering problem context, is a new research topic. We introduce the prediction of similarities between simulations using graph algorithms, which for example allows the identification of outliers or ranks simulations according to their similarities. With that, we address searchability for FE-based crash simulations in the automotive industry. Here, we use SimRank-based methods to predict the similarity of crash simulations using unweighted and weighted bipartite graphs. Motivated by requirements from the engineering application, we introduce SimRankTarget++ an alternative formulation of SimRank++ that performs better for FE simulations. To show the generality of the graph approach, we compare component-based similarities with part-based ones. For that, we introduce a method for automatically detecting components in the vehicle. We use a car sub-model to illustrate the similarity ansatz and present results on data from real-life development stages of an automotive company.

**Keywords:** FE Analysis, Automotive, Searchability, Semantic Data, Outlier Detection, CAE Knowledge, Knowledge Graph, Graph Database, SimRank, SimRank++

## 1 Introduction

The introduction of the semantic web at the beginning of the 20th century resulted in a technology stack to support a 'web of data' rather than a 'web of documents' [18]. In particular, the existence of semantics enhanced searchability as a fundamental functionality to make more use of the data. Further, graph algorithms using interconnectivity and semantics can rank the similarity of the existing entities and predict missing links in

the data. Despite this technological development, many engineering domains still do not exploit semantics and graph modeling to enhance or allow searchability.

In the last decades, computer-aided engineering (CAE) became well established in the R&D process of OEMs in several disciplines. For example, the number of CAE simulations at automotive OEMs are nowadays between 10,000 to 30,000 per week [20]. This amount of data makes CAE in

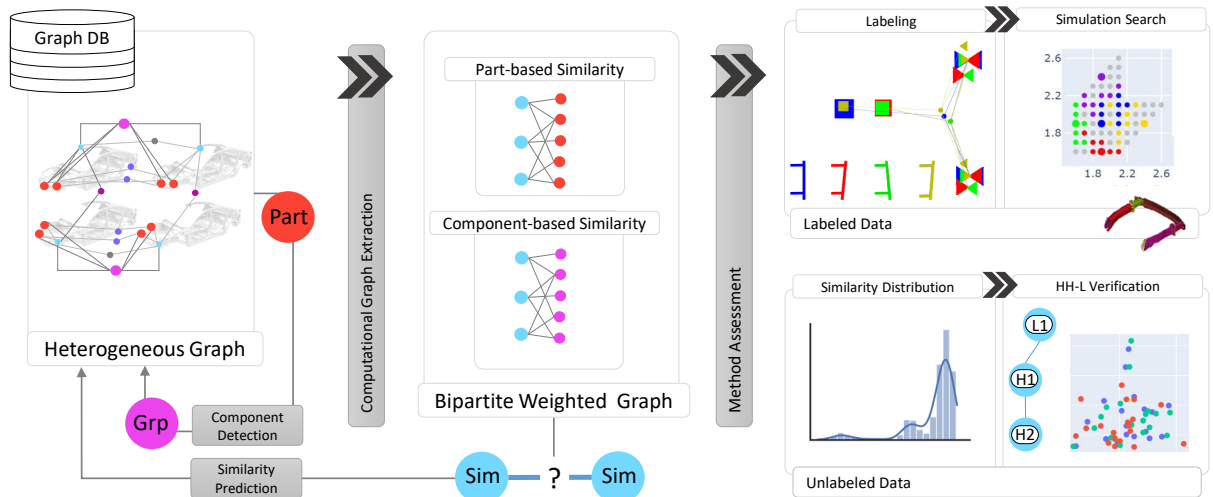


**Figure 1:** Similarity prediction workflow for labeled and unlabeled data. This workflow considers parts and part groups (components) and predicts the similarity based on two variants of a bipartite graph. The nodes' coloring in the heterogeneous graph reflects different node types.

the automotive R&D process one of the engineering domains that can benefit from significantly enhanced searchability. The current lack of sophisticated searchability in CAE data makes the data disconnected and hinders multi-disciplinary collaboration, thereby degrading efficient problem-solving. Additionally, a significant proportion of the available data is not reusable, so it is perceived as so-called dark data [19].

In this work, we introduce enhanced searchability to this domain by assessing graph algorithms to predict similarities of simulations. Predicting the similarity of simulations will assist engineers by allowing a search for the most similar simulations to a given one. Such a similarity connects different design solutions with corresponding behavior, highlights limited explored designs, classifies the studied behaviors, and allows the identification of outliers as those simulations are dissimilar to most others.

Earlier, we established a knowledge graph (KG) for the automotive industry, called car-graph, with a focus on the use case of CAE crash simulations [16, 17]. In this work, we now use semantics to predict the simulations' similarities. The case study is in crash simulations and uses the most energetic parts and derived internal energy features. Nevertheless, one can implement a similar process for other CAE domains after introducing simulation-based semantics that

characterizes the analysis's mechanical properties, e.g., high strain elements for fatigue analysis and eigenmodes structural frequencies for noise-vibration-harshness (NVH) analysis. Currently, no physic-aware methods are available focusing on searchability in CAE simulations to the best of our knowledge.

In this paper, we extend car-graph modeling with link prediction between simulations based on crash behavior that will make the simulations searchable. Car-graph is a heterogeneous weighted graph, and the relations between simulation outcomes are missing. Accordingly, our problem is limited to graph algorithms for unsupervised learning on weighted heterogeneous graphs. Note that labeling the data that will characterize the crash behavior is complex; the behaviors are usually not classified and multi-criterial.

Currently, limited methods are available for unsupervised learning on weighted heterogeneous graphs [13]. Therefore, we reshape our car graph suitable for the best available algorithms. We downsize to a weighted graph with two types of nodes, i.e., a bipartite graph, and employ the widely used SimRank [11] method. This method evaluates the similarity of two types of nodes based on the connectivity of the nodes. To use the edge weights, we also study SimRank++ [2], a SimRank extension that includes edge weights in

the similarity prediction. Furthermore, we introduce a modification of SimRank++ that is better suited for our use case. Note that the graph nodes of our weighted bipartite represent simulations and their main energy absorption entities. Consequently, the commonality of absorption entities between simulations controls the similarity score.

In [17] we introduced energy features for individual parts. With an illustrative example, we motivate energy features as the weights in the bipartite graph. In particular, we can visualize crash simulation behavior in a diagram, label their similarities and classify their behaviors. Further, we investigate a grouping of parts, for which we introduce a method to detect the components in the vehicle automatically, where we take the loading direction of the analysis (impact direction for crash simulation) into account. Therefore, we have two variants for the entity selection in the graph algorithms: the finite element (FE) parts individually and a group of parts representing components.

We examine the performance of predicting similarities in labeled crash behavior from an illustrative example for all the SimRank-based methods. Subsequently, we integrate the proposed part grouping and their energy features into our initial car-graph, which allows an alternative way of predicting similarities between simulations. Finally, we explore our approach on unlabeled industrial data from several development stages in a project of China Euro Vehicle Technology AB (CEVT). Figure 1 summarizes our approach.

In Section 2 we recapture related work, followed by a description of the simulation setups for an illustrative example in Section 3. Then we have an introduction to the SimRank methods and our extension of the method in Section 4. We present our method for component detection in Section 5 and show results for the illustrative example. Next, we introduce an energy diagram that follows the crash behavior in Section 6, and in Section 7 we use these labels to assess the similarity predictions and rankings. Further, we summarize the outcome of similarity prediction for the labeled data, the illustrative example, and unlabeled data (CEVT development stages data) in Section 7. The conclusion and outlook are in Section 8.

## 2 Related work

Dimensionality reduction methods are one of the popular techniques in machine learning (ML) for comparison and gaining an overview of data [14]. In crashworthiness, these methods have been studied since 2008 [1] for exploration and cluster identification [15] of the FE simulations. Note, one can consider the distance of the embeddings as a similarity measure of the simulations. However, the focus of the available research has been on outlier detection or behavior classification [10, 12].

To our knowledge, there is no related work where simulations' similarity is assessed using graph analytics methods. Consequently, we outline other available methods for assessing simulations' similarities. Studies using dimensionality reduction usually look into deformations of the FE model [9, 10, 12, 15, 21]. The challenge with these methods is their computational cost and sensitivity to capture local differences compared with global deformation. For example, these methods focus on realizing an occurrence of a buckling, a global deformation, in comparison to characterizing the buckling mode, e.g., its timing, a local feature. Furthermore, these methods' integration into the OEM's workflow has been limited [21], despite the long period these methods have been available.

Therefore, considering more scalable methods and other input measures is beneficial. One example for crash simulations is the FE solver outputs of energy absorption that gives internal energy (*IE*) per part over time, a so-called energy curve. Studies show that energy absorption characteristics enable quantifying component performance for the design of experiment (DOE) feedback in optimization studies [5, 6]. However, to our knowledge, there is no research on using features generic to the problem, such as energy features, to calculate the similarity of simulations. Another possibility is to use key performance indicators such as firewall intrusion or occupant injury criterion, but these reflect behavior on a much coarser level, which limits their analytical capabilities.

In [17], we investigated features derived from energy curves and studied their capability for summarizing the differences between the simulations. These features have enough resolution to identify the simulations' differences, and the number of parts included plays a role in localizing the

differences. As a result, the differences are more global if more parts are considered compared to including a limited number of parts. Compared to the deformation-based approaches, the main benefit is that these features detect local and global differences. An additional advantage is the computation efficiency that supports more dynamic user interactions.

Another aspect of similarity assessment is FE entities selection for comparison, e.g., node, element, or part. Due to the modeling techniques, most of the FE entities are smaller than a component of the vehicle. Here, a component refers to a group of parts whose structural functionality depends on its parts, e.g., two welded plates of a crash-box, where each plate alone has much less axial stiffness than the welded ones together. Consequently, comparing groups of entities as components can be seen as more physically meaningful.

Note that the grouping information is available in the computer-aided design (CAD) stage of development. However, this data is lost in today's workflow when generating a FE model from CAD information. Detecting these components automatically from a FE model is challenging. In [8], semantics are introduced for FE entities that enable identifying part splits during the development, but the grouping of FE entities from a structural aspect is not addressed. Consequently, we introduce a method to automatically detect the grouping of the FE entities.

### 3 Simulations setups

Using a submodel based on the Yaris FE model from CCSA [4], we generate simulation data that allows easy labeling of the crash behavior. Figure 2a shows the selected components of the submodel, where the main components are the front bumper beam, crash-boxes, and side-members. Accordingly, each simulation includes 28 parts. Originally, the right-hand side (RHS) and left-hand side (LHS) were asymmetric regarding the  $xz$  plane. Therefore, the FE model is modified to make it symmetric. The specific changes consist of removing the toe hook from the RHS, Figure 2c, and making the bumper beam, crash-box and side-member reinforcement symmetrical. To achieve a slight deformation also in the side-members, the side-members end is constrained in  $x$  displacement

and the moment along the  $x$  axis; and a total of 500 kg is added to increase the kinetic energy, Figure 2b.

Our study consists of 66 simulations of a full-frontal impact against a rigid wall with a speed of 56.3 km/h. These simulations have around 30 – 40% increase in total internal energy compared to the complete FE-model. However, the simulation setups for the submodel have minor design changes that are replicating real development process changes. Consequently, the differences in the outcome of the simulation are in the scale of CAE development processes. The simulations vary in crash-box plate thicknesses, where the crash-box is built of two sheet metal thicknesses, Figure 2d. For all simulations, the crash-box outer plate thickness,  $T_1$ , is dependent on the inner plate thickness,  $T_2$ , by

$$T_2 - T_1 = 0.6. \quad (1)$$

Here,  $T_2$  increases from its minimum value in equidistant steps of 0.1 [mm]. These variations are implemented equally on RHS and LHS. In a symmetric setup,  $T_2$  of RHS and LHS increase equally in thickness, while for an asymmetric setup RHS and LHS thicknesses increase unsymmetrically. Figure 3a shows the employed distribution of the  $T_2$  thickness value for LHS and RHS of crash-boxes for 66 simulations<sup>1</sup>.

These changes cause asymmetrical and symmetrical absorption, which results in three crash modes for the deformation, Figure 4. The crash mode indicates the yaw angle of the bumper beam. For this symmetric load-case a symmetric structural stiffness results in a yaw angle of zero. In Figure 3a the simulations with equal thicknesses on LHS and RHS are on the diagonal. For simulations below the diagonal, the LHS is stiffer, causing the crash mode to have a negative yaw  $-v_z$ . For those above, the stiffer RHS causes a positive yaw  $+v_z$  for the crash mode.

Among these 66 simulations, we pick five simulations as reference simulations for the investigation in Section 6. Figure 3b summarizes the crash modes for the selected reference simulations, including one zero mode simulation and two simulations for each negative and positive

---

<sup>1</sup>The simulations and databases are available at: [github.com/Fraunhofer-SCAI/GAE-vehicle-safety](https://github.com/Fraunhofer-SCAI/GAE-vehicle-safety)

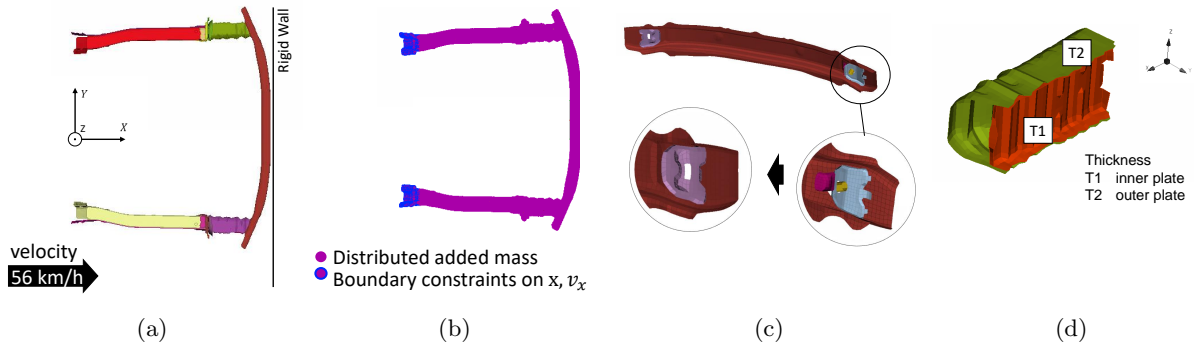


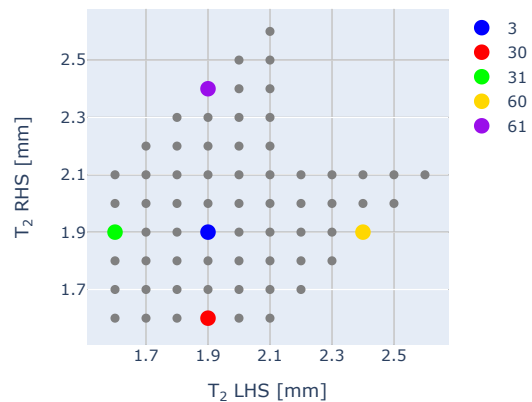
**Figure 2:** FE-sub-model setup, (a) top view of the included components with applying symmetry on crash-box, side-member and bumper beam, (b) add boundary conditions and mass, (c) removing toe hook from the bumper beam. (d) crash-box thickness parameters.

mode. Simulation three is the base model with zero crash mode. The negative and positive modes have mirrored thicknesses, i.e. 30 with 31 and 60 with 61. They also have different stiffness ratios,  $T_{2_{RHS}}/T_{2_{LHS}}$ , i.e. 60-61 is stiffer than 30-31. The reference simulations will later be used to find the most similar ones, see Section 7.

## 4 Simulation similarity prediction

Identifying similar objects based on the link structure in a graph is a fundamental operation in various domains such as web mining, social network analysis, and spam detection [22]. Amid the existing similarity approaches, SimRank [11] has emerged as a powerful tool for assessing structural similarities between two objects. Similar to the well-known PageRank [3], SimRank scores depend merely on the link structure, independent of the textual content of objects. The major difference between the two methods is the scoring mechanism. PageRank assigns an authority weight for each object, whereas SimRank assigns a similarity score between two objects.

SimRank is an approach that is applicable in any domain with object-to-object relationships. It measures the similarity of the structural context in which objects occur, based on their relationships with other objects. Effectively, it computes a measure that says "two objects are similar if they are related to similar objects" [11]. The similarity  $s(a, b) \in [0, 1]$  between objects  $a$  and  $b$  is defined



(a) Spread of thickness  $T_2$  of crash-boxes RHS vs LHS.

Crash Modes					
Ref. Simulations	3	30	31	60	61

(b) Crash modes for the reference simulations.

**Figure 3:** Simulation setup consisting of 66 simulations (a), where five are chosen as reference simulations (b). Colored points in (a) are the reference simulations in (b).

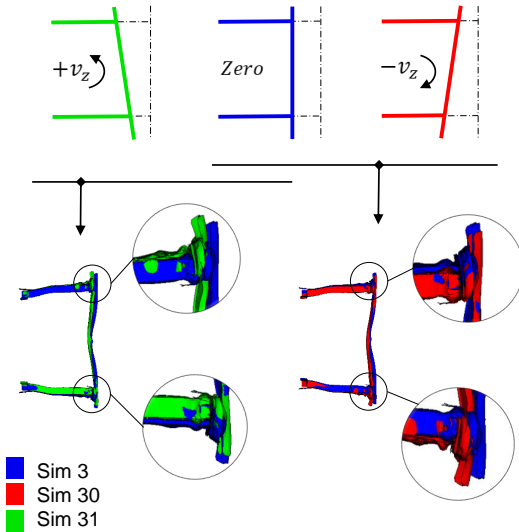


**Figure 4:** Defined label for crash mode based on Yaw axis rotation. FE simulations result follows the color coding of the crash modes.

by a recursive equation. If  $a = b$  then  $s(a, b)$  is defined to be 1, otherwise,

$$s(a, b) = \frac{C}{|E(a)||E(b)|} \sum_{i \in E(a)} \sum_{j \in E(b)} s(i, j), \quad (2)$$

where the set  $E(a)$  contains the edges of node  $a$ , and  $C$  is a constant between 0 and 1.  $C$  gives the rate of decay, since  $C < 1$ , as similarity flows across edges [11] and we use  $C = 0.8$ . In [2], it was shown that SimRank scores are not intuitively correct for complete bipartite graphs<sup>2</sup>. In our application, we typically obtain a complete energy bipartite graph and have edge weights.

To work well with complete bipartite graphs, [2] introduced SimRank++, a so-called evidence-based SimRank, which additionally uses edge weights and the so-called spread to achieve similarity scores consistent with the graph's weights. In particular, [2] introduces the notion of evidence

<sup>2</sup>Note that, a complete bipartite graph is a bipartite graph, where every vertex of the first node-set connects to every vertex of the second node-set.

of similarity between nodes  $a$  and  $b$

$$evidence(a, b) := e_{a,b} := \frac{|E(a) \cap E(b)|}{\sum_{i=1} 2^i} \frac{1}{2^i} \quad (3)$$

as an increasing function in the number of common neighbors. Further, using normalization and scaling according to the local variance, one obtains weights  $W$

$$W_{a,i} = \underbrace{e^{-\text{variance}(i)}}_{\text{spread}(i)} \frac{w(a, i)}{\underbrace{\sum_{j \in E(a)} w(a, j)}_{\text{normalized\_weight}(a,i)}}, \quad (4)$$

where  $\text{variance}(i)$  is the variance of the edge weights  $w$  of node  $i$ . All together, SimRank++ utilizes the edge weights to compute similarity scores iteratively by

$$s^{++}(a, b) = e_{a,b} \cdot C \sum_{i \in E(a)} \sum_{j \in E(b)} W_{a,i} W_{b,j} s^{++}(i, j).$$

We observe that SimRank++ normalizes the edges that have a common source node. A pair of nodes  $(v, w) \in V \times V$  is associated with every edge  $e \in E$ ;  $v$  is called the source of  $e$  and  $w$  is called the target of  $e$ , where  $V$  is a list of nodes and  $E$  is a list of edges in a graph. Alternatively, we propose to normalize the weights with a common target node, which we call SimRankTarget++ ( $s_{trgt}^{++}$ ). We believe that, depending on the physical meaning of the source and target, it matters how the weights are normalized. This modification enables the iterative method to calculate the distribution of one target for all the sources instead of all targets' distribution in one source. We will discuss this further in Section 7.2. Consequently, we introduce  $Q$ , where we normalize the edges concerning the target nodes

$$Q_{a,i} = \underbrace{e^{-\text{variance}(i)}}_{\text{spread}(i)} \frac{w(a, i)}{\underbrace{\sum_{j \in E(i)} w(i, j)}_{\text{normalized\_weight}(a,i)}}, \quad (5)$$

and using  $Q$  we define iteratively

$$s_{trgt}^{++}(a, b) = e_{a,b} \cdot C \sum_{i \in E(a)} \sum_{j \in E(b)} Q_{a,i} Q_{b,j} s_{trgt}^{++}(i, j).$$



## 5 Component detection

FE-modeling techniques require arranging vehicle components into several parts, e.g., due to material and thickness differences<sup>3</sup>. Consequently, FE-solvers output result quantities per defined parts. This split makes the post-processing of the results per component challenging. Since the parts connectivities as a component are unavailable, it is vital to develop a method for component detection to facilitate post-processing.

With components, we refer to a group of parts that in their structural analysis from a CAE analysis perspective are highly dependent. For example, the stiffness of the side-member component, (F) in Figure 5, depends on three reinforcement plates as well as the inner and outer side-members. One application of using components is in selecting the most essential parts for ML pipelines. In [17], we showed that using the maximum of the internal energy is capable to filter the essential parts. However, this approach sometimes excludes smaller parts that are of interest from crashworthiness aspects, e.g., the reinforcement plates, (l), (m), (n) in Figure 5.

In this section, we propose a method for component detection, verify its outcome for the illustrative example and discuss its scalability. Finally, we discuss options for evaluating energy features for components.

### 5.1 Component detection method

There are several possibilities for component detection. One option is to preserve this information from CAD to CAE by introducing a corresponding workflow within the company. However, this option is for now not feasible due to the involved process dependencies that are time-consuming to establish in big OEMs. A second approach is to develop an interpreter for the specific FE solver that transfers each connection type to a generic connection for component buildup. In [16], we partially employed this method to identify connection changes in the model. The limitations of this approach are: a) time-consuming development due to the dependencies on the specific solver and b) the need to use several modeling representations for different types of connections.

Additionally, recent computational power allowed FE-models to include more details. As a result, connectivities, e.g., bolts and clips, are modeled with generic FE entities, e.g., shell solid elements, instead of a solver-specific abstraction for connections. Therefore, developing the interpreter would be even more complicated. Moreover, both outlined approaches deliver several connections per pair of parts due to assembly requirements, e.g., several bolting or welding. The high number of connections requires additional filtering to distinguish a component's assembly from a component-to-component connection. Thus, a more automatic method is beneficial.

Therefore, we develop a geometrical search method that detects components. We consider each part in the vehicle as a box and then group highly overlapped boxes. The geometrical features of the parts define the box, including length, width, and height, along with the coordinate system of the FE-model (L-x, W-y, H-z). In grouping these boxes, we make the following procedural decisions

- Include specific entities from the FE-model<sup>4</sup>.
- Define FE-modeling guidelines to differentiate parts from connections<sup>5</sup>.
- Decide on a box merge in a pairwise comparison.
- Define batches for pairwise comparison via two-dimensional (2D) k-means clustering<sup>6</sup> to reduce computational time.
- Consider two-stages in merging: complete and partial overlap. Complete overlap is the scenario, where a smaller box (child) is located entirely in a bigger box (parent). By contrast, partial overlap refers to situations where boxes are not completely overlapped.
- Skip merges in the direction of the impact/loading for partial overlapping to capture the load path.

We start the investigation on the FE-submodel presented as an illustrative example, in Section 3. This model includes 28 parts, and 27 parts match the prescribed entity selection. From

---

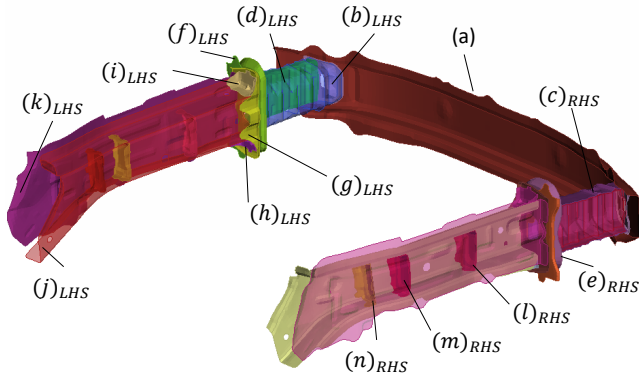
<sup>4</sup>Only shell elements since beam and solid elements usually represent the connections and have a single properties ID (PID) for all same type of connection in the model.

<sup>5</sup>Require null shell elements for components modeled with solid elements. null shell is a recommended method for better contact modeling, MAT\_NULL in LS-DYNA.

<sup>6</sup>Using the implementation from, `sklearn.cluster.KMeans` python package.

---

<sup>3</sup>For further background on crashworthiness, see e.g. [7].



(A) bumper beam	(a) bumper beam (b) frame front cap
(B) crash-box	(c) crash-box inner (d) crash-box outer
(C) connector plate 1	(e) connector plate 1
(D) connector plate 2	(f) connector plate 2
(E) connector plate 3	(g) connector plate 3 (h) reinforcement 1 (i) reinforcement 2
(F) side-member	(j) side-member inner (k) side-member outer (l) side-member reinforcement 1 (m) side-member reinforcement 2 (n) side-member reinforcement 3

**Figure 5:** Grouped component for the FE sub-model, 27 parts and eleven corresponding components. In the table, uppercase letters are referring to the component and lowercase letters to the parts. In the figure, only one of the symmetric parts is marked and correspondingly subscripted with either LHS or RHS.

the crash analysis engineering view, this model contains eleven components: (A) bumper beam, (B) crash-boxes on right hand side (RHS) and left hand side (LHS), (C)(D)(E) connector plates on RHS and LHS, and (F) side-members on RHS and LHS. Thus, the intended outcome is eleven components. Connector plates between crash boxes and side members could be one component. However, as mentioned, in our grouping procedure, we prevent merging boxes with overlaps in the direction of the impact/loading.

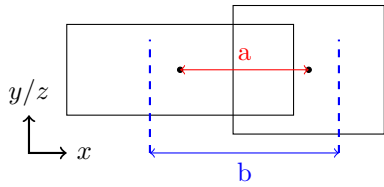
For grouping boxes, we compare boxes pairwise. Pairwise comparison of all parts for the complete FE-model is computationally expensive. Therefore, we use k-means clustering<sup>6</sup> on the boxes' center of gravity (COG). Pairwise comparison takes 346 seconds for the complete model of Yaris with 728 initial parts, and with k-means clustering, we reduce the time to 23 seconds. In this way, the clustering of the boxes creates batches to reduce the number of pairwise comparisons. We consider the boxes COG distances in pairwise comparison. However, the three-dimensional (3D) distance of parts clusters the parts locally and will skip some desired merges.

For example, the bumper beam component in Figure 5 (A) will encounter this issue since the bumper beam, part (a), and the RHS and LHS frame front cap, part (b), have a significant COG

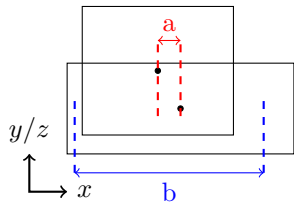
distance in 3D space. In this example, the 3D distance will cluster the frame front cap with the crash-box, not the bumper beam. Consequently, we consider the 2D space for clustering the boxes and assess each separately, top-view ( $xy$ ), front-view ( $zy$ ), and side-view ( $xz$ ). In this example, the bumper-beam and the frame front cap have an apparent distance in the top-view and front-view clusters, these boxes will not be compared. However, the boxes COG are close in the side-view, and will be in the same cluster to be assessed. As a result, we have an additional iteration loop to assure all required pairs are assessed, in each loop we are switching between 2D views to change the clustering. After several iterations, we compare all remaining parts pairwise to be sure all boxes have been compared.

The pairwise comparison investigates two scenarios: complete and partial overlap. Complete overlap is when a box is entirely inside a larger box. Here, the merged box takes over the dimensions of the larger box. For partial overlap, we use as the comparison quantity

$$\frac{\overbrace{|c_{cog_{b_1}} - c_{cog_{b_2}}|}^a}{\underbrace{(L_{cb_1} + L_{cb_2})/2}_b} \leq T, \quad (6)$$



(a) Partial overlap in impact direction,  $x$ , classified in impact direction and not approved for merge.



(b) Complete overlap in impact direction,  $x$ , not classified in impact direction and will go to the next check for merging.

**Figure 6:** Two examples of classifying the overlaps in direction of the impact with big and small distances of  $\alpha := a/b$ , subfigure (a) and (b) respectively.

i.e., the fraction of the COG distance and the average of the boxes' side lengths in the chosen direction.

$c_{cogb_1}$  and  $c_{cogb_2}$  are the COG coordinates component for the compared boxes, box one and two respectively. The coordinate components are in the global axis direction:  $x$ ,  $y$ , and  $z$ . The  $L_{cb_1}$  and  $L_{cb_2}$  are the box dimensions in the corresponding axis, for boxes one and two respectively. The dimension  $L_c$  is aligned with global axis:  $L_x$ ,  $L_y$ , and  $L_z$ .

The threshold  $T$  in equation 6 is used for two scenarios, classifying the overlaps in impact direction and deciding on overlap merging. Therefore, two different thresholds are applied for each scenario:  $\alpha$  and  $\beta$ , respectively. For impact direction classification, threshold  $\alpha$  is set to a low value, e.g., 0.01, which prevents box merging for  $a/b$  bigger than this value, Figure 6a. Afterward, if the overlap is not classified in the impact direction, its percentage of overlap is evaluated to decide on boxes merging. For overlap check, the impact plane directions are assessed with the threshold  $\beta$  set close to one, e.g., 0.97, Figure 6b. Here the

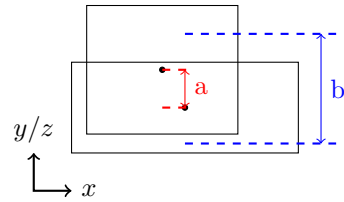


**Figure 7:** Decision making of box-merge in impact plane,  $yz$ .

boxes will merge for a large ratio of  $a/b$ , Figure 7. In full-frontal impact in the  $x$  plane, considered overlaps are in the  $y$  and  $z$  plane.

---

#### Algorithm 1 Box merge for impact direction $x$

---

```

if  $a_x/b_x \leq \alpha$  and  $a_x > 0$  then
  if  $a_y/b_y \leq \beta$  and  $a_z/b_z \leq \beta$  then
    merge boxes
  end if
end if

```

---

## 5.2 Component verification

The outcome of this method for the illustrative example matches the table in Figure 5. Initially, 27 boxes represent the 27 parts and after merging eleven new boxes are generated that include the parts as in Figure 5. Here we run the merging for the frontal impact that will skip the merges in the  $x$ -direction; see the coordinate system in Figure 2a. Consequently, the connector plates even with the existing overlap in the  $x$ -direction are not merged, components C, D, and E.

Afterward, we implement this method on the full Yaris model to assess the scalability of this method. One obstacle in the full model application is the dominance of the exterior parts that is acting as a wrapper for a big proportion of the parts, e.g., the front facia and outer layer of the vehicle body. A solution for this is to exclude the exterior parts defined by the user. An additional option is to combine part filtering with grouping as,

- Filter the most energetic parts.
- Apply the component detection with the limited search for filtered energetic parts and their neighbors.
- Update the filtering with the most energetic components.

In this way, the focus will remain on the structural parts and exterior parts will not cause an issue.

### 5.3 Component features

In [17], we introduced energy features for the  $IE$  of each part with initial absorption time  $[t_i]$ , maximum internal energy  $[IE_{max}]$ , and end of absorption time  $[t_n]$ . Since these features are part-based, enabling the post-processing of the results at the component level requires an additional step to combine the features. Two approaches exist to generate component-based features. First, combining the features of the grouped parts belonging to a component. Here, combining features refers to determining the minimum, maximum, sum or average of a group of features. The other alternative is summing up the parts' curves before feature extraction.

For  $IE$  curves, the outcome of these two approaches affects the time features more noticeably. For  $IE_{max}$ , the effect is minor since  $IE$  saturates after the maximum. Consequently, the sum of  $IE_{max}$  for parts and max of  $IE$  summation curve differs only slightly. However, the  $t_i$  and  $t_n$  features deviate more between the two approaches. In curve summation, the early ramp-up or late saturation of the  $IE$  vanishes for the parts with the smaller energy due to the dominance of the more energetic parts. As a result, we propose to use the part combined features for the time features,  $t_i$  and  $t_n$  minimum and maximum respectively, while using  $IE_{max}$  from the summation curve.

## 6 Energy diagram

We introduce an energy diagram to illustrate simulation behaviors in a crash simulation. For simplification, we have a 2D view using  $IE_{max}$  and  $t_n$ , where  $t_n$  contains the  $t_i$  feature and relates to absorption time,  $\Delta t = t_n - t_i$ . An additional benefit of  $t_n$  is that it is easier to understand visually than  $\Delta t$  for processing the sequence of behaviors, i.e., the part's relative behavior [17]. To shape the energy diagram, we select the five most energetic parts for each simulation and add the mean of energy features to the plot and connect each part. Note that, considering the 28 parts included in each simulation of the illustrative example will make the visualization challenging. The five parts

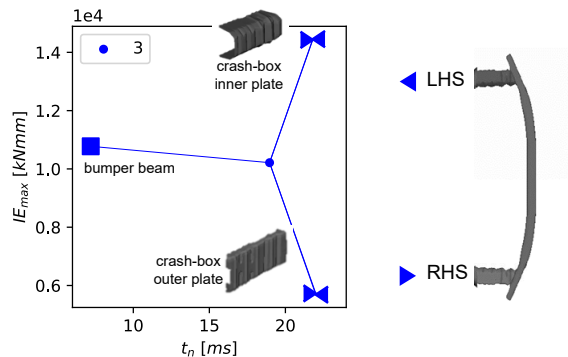


**Figure 8:** Base simulation energy diagram, considering five parts, base simulation in Section 3.

turn out to be the same for all simulations, including the four plates of the crash-box and the bumper beam.

### 6.1 Diagram examples

Figure 8 shows the energy diagram for the base simulation. Left and right directed arrows indicate the LHS and RHS parts of the crash box, respectively, where a square represents the bumper beam. The final energy diagram is obtained by connecting each part to a point reflecting the average of the energy features of the five parts.

Figure 9a displays the energy diagrams for simulations 30 and 31. These simulations have the same thickness value change but on opposite sides. As a result, the corresponding energy diagrams are essentially mirrored. Their structures look identical except for the switch between RHS/LHS, reflecting the change in producing negative or positive yaw. In Figure 9b we compare one of these mirrored simulations to the base model. We observe that the  $IE_{max}$  has decreased for RHS crash-box plates, which is due to the stiffness reduction. However, in comparison,  $t_n$  has not changed. The reduction of  $IE_{max}$  while  $t_n$  is unchanged indicates a so-called stack-up state<sup>7</sup>. However, the average of the energy features shows lower  $IE_{max}$ . Therefore, the side-members are absorbing the remaining energy since the total  $IE$  should remain the same over all the parts in the simulation. Another noticeable observation is that the bumper beam absorption energy

<sup>7</sup>Maximum possible deformation in a component.

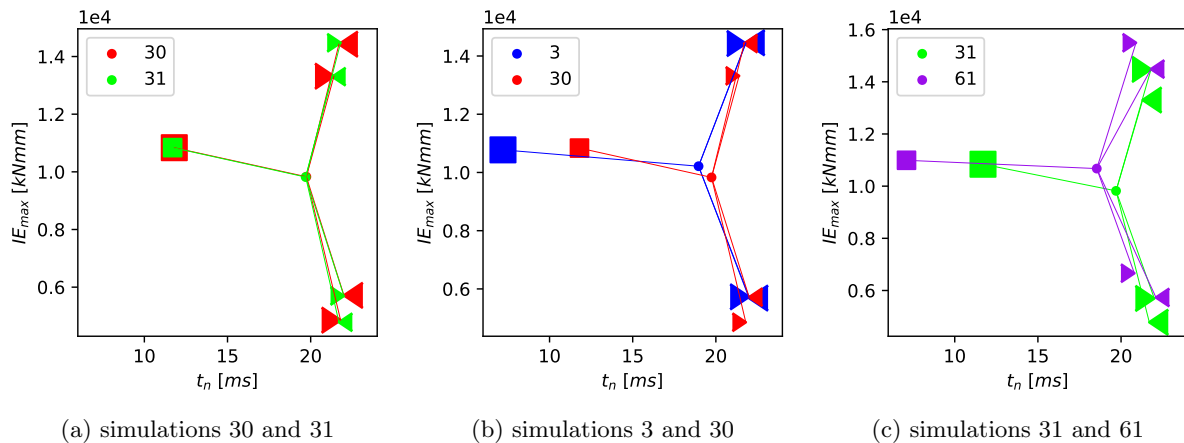


**Figure 9:** Energy graph for simulations in Section 3, crash mode defined based on Yaw axis rotation.

is independent of crash-box, however, the  $t_n$  is dependent.

Figure 9c presents the energy diagrams for simulations 31 and 61, wherein both the RHS crash-box is stiffer than the LHS resulting in the negative yaw crash mode. We observe an offset in the diagrams, while the structures are similar since they reflect the similarity of the crash mode. The angle differences in each energy diagram correspond to the yaw angle. Note, the offset is due to more energy absorption in simulation 61, reflecting its higher thickness values.

## 6.2 Diagram similarities

Representing simulations as a diagram with energy features enables the comparison of simulations. The illustrative example highlights two scenarios: a change in the diagram’s structure and an offset of the whole diagram. From an engineer’s perspective, these two aspects can be considered as crash mode and absorption factor. First, a crash mode reflects the parts’ absorption relative to each other, represented by the diagram’s structure. On the other hand, one looks at how much energy is absorbed with the absorption factor. Thus, the absorption factor operates as an offset factor in the energy diagrams in this data representation. Consequently, the same crash mode but different absorption factors exist if the relative stiffness of the components is similar.

With these visual definitions of similarity between simulations using energy diagrams, we have the following research question: how to implement

these in graph analytic methods to estimate simulation similarities? Working with unsupervised learning methods on these energy diagrams would involve treating these as separate data objects and individual weighted graphs, an ongoing open research question [23]. Instead, we investigate the energy features as weights in a graph to be able to use established methods for link prediction. In this way, we use the edge weights to detect slight differences between simulations as presented in examples we discussed in Section 6.1.

## 7 Similarity results

In this section, we present and compare different SimRank methods for predicting the simulation’s similarities. We start with a short description of our bipartite graph, both part-based and component-based, and its connection to our graph database [16]. Afterward, we evaluate SimRank methods and compare them with the root mean square error (RMSE) of displacements and internal energy as a similarity baseline. We use two approaches for evaluating the similarity predictions:

- Comparing a labeled ranking, where we order the five reference simulations from an engineering perspective and compare this ranking with one based on the computed similarities.
- Searching for similar simulations, where for the five reference simulations we find the most similar ones among the remaining 61 simulations.

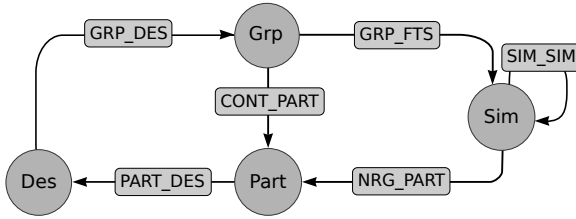


**Figure 10:** Graph data schema used for simulations similarity prediction, full schema available in [16].

Finally, we present results from an industrial application of this method.

## 7.1 Bipartite graph

Let us provide a brief overview of our graph modeling for both part- and component-based bipartite graphs. Figure 10 shows the data schema that we here employ, which is part of the entire graph modeling we introduced in [16]. In this schema, a  $\text{Sim}$  node reflects a FE simulation outcome, where its properties stem from global entities of the simulation, e.g., total mass or impact energy. An FE-model contains many elements, where a group of elements with the same properties is identified as one part. Consequently, one simulation includes several parts and we model it with a  $\text{Part}$  node as the main entity representing the simulation. The edge  $\text{Part} \text{---} \text{NRG\_PART} \text{---} \text{Sim}$  relates  $\text{Part}$  nodes to  $\text{Sim}$  nodes and includes certain energy features of the parts as weights. Design  $\text{Des}$  nodes bundles parts that have similar FE-model features. A  $\text{Grp}$  node is a group of different  $\text{Part}$  nodes in the database that reflect the outcome of our component detection method.

For simulations similarity prediction, we are looking to predict the  $\text{Sim} \text{---} \text{SIM\_SIM} \text{---} \text{Sim}$  edge. Both bipartite graphs, part- and component-based, respectively, have with  $\text{Sim}$  and  $\text{Des}$  two node types, see Figure 11 for the part-based graph. Therefore, the similarity of connections between  $\text{Sim} \text{---} \text{Des}$  is used to predict a  $\text{Sim} \text{---} \text{Sim}$  connection. We have two scenarios for structuring the bipartite graph with  $\text{Sim} \text{---} \text{SIM\_DES} \text{---} \text{Des}$ . First, for the part-based similarity, we follow  $\text{Sim} \text{---} \text{NRG\_PART} \text{---} \text{Part} \text{---} \text{PART\_DES} \text{---} \text{Des}$ . Here, we obtain the edge weight from the parts' energy features and predict the simulations' similarity

PID		Part Name
2000000		bumper beam
LHS	RHS	
2000001	2000501	crash-box inner plate
2000002	2000502	crash-box outer plate

**Table 1:** Part names for PID in Figure 11.

based on the parts' absorption similarity. Second, for the component-based similarity, we go along  $\text{Sim} \text{---} \text{GRP\_FTS} \text{---} \text{Grp} \text{---} \text{GRP\_DES} \text{---} \text{Des}$  and use the grouped features as weights and predict the simulations' similarities based on the components absorption similarities.

## 7.2 Part-based similarity

To study part-based similarity, we compare the results from different SimRank formulations with a defined labeled ranking for the Yaris simulations from Section 3. Table 2 summarizes the results. In this table, we order the columns according to the desired ranking based on engineering judgment as follows:

- Simulations  $\text{30}$ – $\text{31}$  are the most similar due to the symmetric changes.
- Simulations  $\text{3}$ – $\text{61}$  are the least similar since there is the most significant stiffness change among all simulations.
- The pairwise similarity of  $\text{30}$  or  $\text{31}$  to simulations  $\text{3}$  and  $\text{61}$  should be equal. Equality comes from symmetrical behavior that acts as a mirrored weight on nodes.
- Simulations  $\text{30}$  and  $\text{31}$  are more similar to  $\text{3}$  than  $\text{61}$  since the stiffness difference is less in  $\text{3}$ – $\text{31}/\text{30}$  compared to  $\text{61}$ – $\text{31}/\text{30}$ . As a result, simulations  $\text{3}$ – $\text{30}$  and  $\text{3}$ – $\text{31}$  have the second-order ranking with equal values, and simulations  $\text{61}$ – $\text{31}$  and  $\text{30}$ – $\text{31}$  have the third-order ranking.

The used methods include SimRank ( $s$ ), weighted SimRank ( $s_w$ ), weighted SimRank with evidence ( $s_{w, evd}$ ), weighted SimRank with evidence and spread ( $s^{++}$ ), and weighted SimRank with evidence and spread that is normalized over target nodes ( $s_{trgt}^{++}$ ). We employ the energy power absorption ( $P_e = IE_{max}/\Delta t$ ) of the parts as the weight for the  $\text{Sim} \text{---} \text{SIM\_DES} \text{---} \text{Sim}$  edges. Another



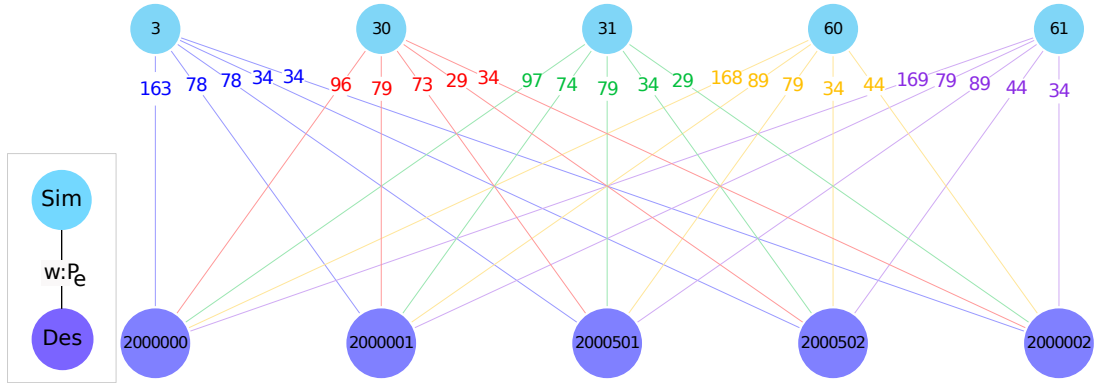


**Figure 11:** Bipartite graph for illustrative example with  $P_e$  as edge weight, shown values are in  $[10MNm/s]$ . The edge color follows reference simulations in Section 3.

Method	30-31	3-30	3-31	61-31	61-30	3-61
s	0.4444	0.4444	0.4444	0.4444	0.4444	0.4444
$s_w$	0.4749	0.4795	0.4798	0.4789	0.4783	0.4892
	6	3	2	4	5	1
$s_{w,evd}$	0.4379	0.4427	0.4430	0.4420	0.4414	0.4527
	6	3	2	4	5	1
$s^{++}$	0.2084	0.2104	0.2102	0.2267	0.2260	0.2295
	6	4	5	2	3	1
$s_{trgt}^{++}$	0.3119	0.2719	0.2717	0.2695	0.2695	0.2399
	1	2	3	4	5	6

**Table 2:** Similarity prediction from different methods when considering the five most energetic parts in the illustrative example, Figure 11. The order of columns is the expected order as described in Section 7.2, ( $C = 0.8$ ,  $weight = P_e$ ).

Scalar	Time Step	Parts	30-31	3-30	3-31	61-31	61-30	3-61
	$t_{max}$	All	5.55	7.60	7.82	21.16	21.96	15.25
			1	2	3	5	6	4
Displ	$t_{all}$	All	7.97	7.02	7.09	17.35	20.45	13.82
			3	1	2	5	6	4
	$t_{max}$	Five energetic	5.92	4.74	4.67	9.06	9.83	6.03
			3	2	1	5	6	4
$P_e$	$t_n$	All	4.5	299.1	295.1	327.5	331.3	69.5
			1	4	3	5	6	2

**Table 3:** RMSE for the difference of displacement ( $Disp [mm]$ ) and  $P_e$  ( $([MNm/s])$ ) in each pair of simulations, considering a different number of parts and time steps in the illustrative example. The even rows show the ranking of the distances. The order of columns is the expected order described in Section 7.2.

alternative for the edge weight is the  $IE_{max}$ ; however,  $P_e$  gives better results. In the study, we select the five most energetic parts, which are the bumper beam and two plates of the crash-box on LHS and RHS, Table 1.

Table 2 presents the  $\textcircled{\text{Sim}}-\textcircled{\text{Sim}}$  similarity predictions<sup>8</sup> for the illustrative example. Figure 11 shows the five most energetic parts for the five simulations. This results in a fully bipartite graph, and disregarding weights means that two simulations are similar if the energetic parts are similar. Therefore, as expected from Section 4, SimRank predicts that all simulations are similar, which shows that the method is insufficient to evaluate the similarity between simulations with similar energetic parts but different absorption distributions.

With the  $P_e$  weight, the predicted similarities still differ from our expectations for  $s_w$ ,  $s_{w,evd}$  and  $s^{++}$ . However, the  $s_{trgt}^{++}$  method provides a result that reflects our labeling. Note that to observe an effect using the weight factors, they need to be scaled to be smaller than 2 ( $P_e$  scaled with  $10e8$  based on this model unit system, energy  $[N-mm]$  and time  $[s]$ ). If the spread is more expansive than two, then all similarities become zero, and if it is smaller than one, the result is similar to the weighted graph without spread.

It is interesting to further discuss the difference of  $s_{trgt}^{++}$  and  $s^{++}$  in this use case. Considering  $s^{++}$  and normalizing the edges regarding the sum of the edges in the source nodes refers to normalizing each part absorption with the total IE in a model, which is more or less constant for all the simulations when considering one load-case. However, normalizing for edges in the target nodes, we are normalizing the edge weight with the total absorbed energy for that specific part in all simulations, which highlights the absorption efficiency of that part for each simulation. Consequently, the second approach is more relevant for comparing simulations since we can weigh the parts' relative to each other instead of the first approach, which looks into the parts' relativity in one simulation.

To further study the performance of the proposed algorithm, we compare with rankings based on similarity or distance measures for simulations.

A common approach is to assess differences in the simulations is by looking at mesh-based function differences, e.g., [10, 9]. Therefore, we use the differences in the displacement between the simulations and use the RMSE as the distance. Table 3 summarizes the RSME of the displacements and the corresponding ranking for the illustrative example in three scenarios: all parts at the last time step  $t_{max}$ , all parts in all the time steps, and the five most energetic parts in the last time step. From Table 3 we gather that none of three approaches can capture the expected crash behavior in the order prescribed previously. The top three and the last three similarities are invariant. However, there is a different order within each cluster. Differences in the ranking show that this method is time-step dependent. Additionally, parts meshes should be the same to be able to evaluate the RMSE. Further, looking at all time steps is computationally expensive, and the time sequence of events can lead to high differences while the final crash mode is similar, e.g., stack-up situations. While looking at only the last step would solve this issue, but the sequences of events will still be missing in the similarity calculation.

Another approach is to evaluate the RMSE for the internal energy of the parts with more global features than displacement, the last row in Table 3. Here for simulation pairs,  $P_e$  are compared for the five most energetic parts. The main difference is the ranking of  $\textcircled{3}-\textcircled{61}$  as the second.

So far, we have investigated different configurations of the SimRank++ method for similarity prediction between simulations. An additional hyperparameter to evaluate is the number of employed parts from each simulation that are used in the bipartite graph. Table 4 summarizes  $s_{trgt}^{++}$  prediction for 2, 5, 15, and 28 (all) parts being considered. The order of the predicted similarity between simulations has the expected pattern for the labeled data upwards from including five parts. Noteworthy, the similarity score spread declines when including more parts.

### 7.3 Component-based similarity

Initially, we constructed a bipartite graph based on the FE parts to predict the similarity of simulations. We now consider similarity predictions based on the components, where we use the outcome of the component detection presented in

---

<sup>8</sup>We modify the SimRank similarity calculation in the NetworkX Python package to evidence-based SimRank with spread consideration.



No. Parts	30-31	3-30	3-31	61-31	61-30	3-61	Range
2	0.4239	0.4243	0.4243	0.4235	0.4228	0.4234	0.0016
5	0.3119	0.2719	0.2717	0.2695	0.2695	0.2399	0.0719
15	0.2763	0.2568	0.2565	0.2518	0.2517	0.2393	0.0370
28	0.3086	0.2976	0.2973	0.2947	0.2945	0.2902	0.0184

**Table 4:** Part-based  $s_{trgt}^{++}$  similarity prediction deviation regarding changing the number of energetic parts included in the illustrative example, Figure 11, ( $C = 0.8$ ,  $weight = P_e$ ).

No. Parts	30-31	3-30	3-31	61-31	61-30	3-61	Range
2	0.4198	0.4211	0.4212	0.4180	0.4166	0.4182	0.0046
3	0.4125	0.4071	0.4071	0.4009	0.4003	0.3967	0.0157
5	0.2440	0.2260	0.2262	0.1997	0.1990	0.1858	0.0583
11	0.2517	0.2394	0.2395	0.2266	0.2260	0.2166	0.0351

**Table 5:** Component-based  $s_{trgt}^{++}$  similarity prediction deviation regarding changing the number of energetic components included in the illustrative example, ( $C = 0.8$ ,  $weight = P_e$ ).

Section 5. Table 4 summarizes the prediction result of  $s_{trgt}^{++}$  for the component-based bipartite graph while increasing the number of most energetic components included. This evaluation requires at least three components to fulfill the previous section’s pre-defined ranking. Parts included in these three components are similar to the five parts in similarity prediction of Table 4. However, using components, the predicted similarities have higher values.

Additionally, for the component-based similarity, the maximum range of the spread is achieved by including five components, 15 parts, whereas for part-based similarity, it is with five parts. Note that the 15 parts involved in component-based similarity are not equivalent to 15 parts in part-based similarity. Six parts are the side-member reinforcement plates when filtering with components and are not selected as the most energetic parts when using parts. Consequently, component-based similarity performs adequately with a more stable result; however, the part-based similarity is more sensitive.

Moreover, the similarity range drops less with increasing the number of components than with the number of parts. If we compare the full model prediction, 28 parts for the part-based compared with eleven components, the component-based has a broader range than the part-based. Overall component-based similarity shows better results in this use case.

## 7.4 Searching simulations

In this section, we use the similarity prediction methods to search for simulations similar to the five reference simulations. First, we compare the capabilities of the  $s_{trgt}^{++}$  and RMSE of  $P_e$  methods as a search tool. In Figure 12 we visualize for each of the reference simulations from Section 3 the corresponding top seven similar simulations. We expect to have the diagonal points,  $x = y$ , similar to simulation three with zero modes. This is because the points have the same relativity of the thickness of the crash-box plates. Likewise, the simulations under  $x = y$  should be similar to simulations 30 and 60 and mode  $+v_z$  based on their stiffness range, while the ones above should have mode  $-v_z$ . Figure 12a shows that the  $s_{trgt}^{++}$  method achieves the expected clustering, e.g., the modes stay on one side of the diagonal. On the other hand, Figure 12b shows that the RMSE of  $P_e$  method fails to recognize the crash modes as the colored points for simulations 30, 31, 60, and 61 are on both sides of the diagonal. This result shows that this method primarily works by averaging the parts’ energy absorption.

Next, we compare part-based and component-based results. Figure 13 visualizes the comparison of the two methods while increasing the number of target nodes in the bipartite graph,  $\textcircled{\text{Part}}$  and  $\textcircled{\text{Grp}}$  for part-based and component-based methods, respectively. This comparison also highlights

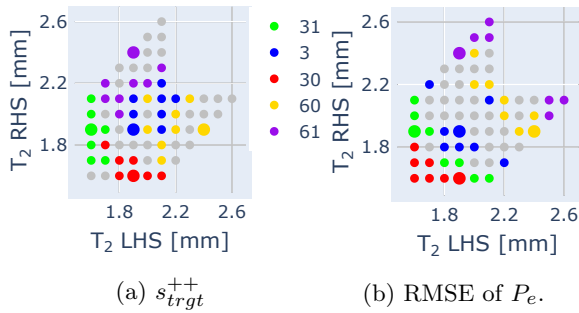


**Figure 12:** Most similar simulations to the reference simulations according to two similarity estimations. The used color code of simulations is from Section 3.

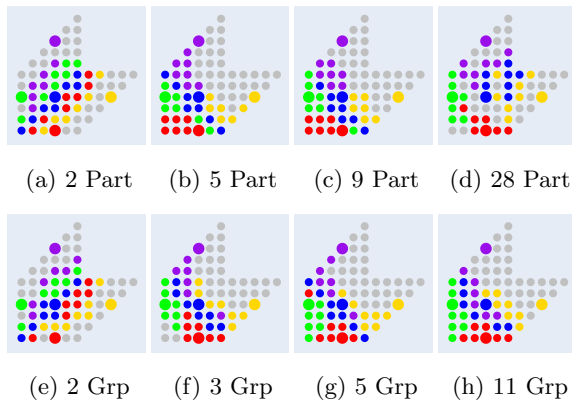


**Figure 13:** Comparing part-based labeling (a)(b)(c)(d) with component-based (e)(f)(g)(h) while varying the number of  $\text{\textcircled{Part}}$  and  $\text{\textcircled{Grp}}$  nodes respectively. x-axis, y-axis, and coloring are the same as in Figure 12.

the deviation between the two methods by increasing the number of parts. Additionally, the color coding for the zero mode deformation, blue scatter points, is captured the best for the minimum included target nodes, Figure 13a, 13e. This observation emphasizes that finding a similar simulation differs from ordering the similarities. For finding the most similar simulation, including the least number of target nodes or part-based assessment, perform satisfactorily. However, from the robustness aspect and the ranking of the prediction, the component-based is more promising.

## 7.5 Industrial application

After investigating the SimRank++ method for the illustrative example, we apply the approach to data from CEVT, using the so far best-performing configuration, i.e., SimRankTarget++. This data includes a total of 611 simulations of three different load-cases from frontal impact (ffo: full front overload, foU: front oblique overlap, and foI: front small overlap) in four successive development stages (primary, early, middle, and late)<sup>9</sup>.

For this data, the bipartite graph is part-based with energy power as the weight factor,  $P_e = IE_{max}/\Delta t$ . The similarity prediction considers each load-case for each development stage separately for a specified number of parts, i.e., 20. The load-case separation of simulations is due to the use-case that similarity between different load-cases is usually out of interest. Furthermore, the grouping of development stages is due to PID changes between development stages to avoid connecting two irrelevant parts. The necessary parts mainly vary between load-cases and slightly among developmental stages.

Here we present an overview of these results and deep dive into the result for one load-case in a single development stage. The industrial data is unlabeled, so it is challenging to assess the result of the similarity predictions. To tackle this, we introduce two approaches. First, we visualize the similarity prediction result using a histogram and a KDE<sup>10</sup>. Second, we select specific simulation pairs in each batch to further analyse the similarity prediction, H-LL simulations. We present these approaches for the foI load-case in the primary development stage.

### 7.5.1 Similarity density

The similarity prediction score depends on the selection of simulations in the batch and the number of included designs. Figure 14 presents the similarity distribution for different load-cases in different development stages. Here, we analyse each load-case in separate development stages. Each calculation is without simulations with similarities of less than 0.2. The KDE plots the probability of data being in a given range in the area under the density curve. The KDE graph's

<sup>9</sup>Detailed data description in Section 3 of [17].

<sup>10</sup>seaborn.distplot python package with KDE=True

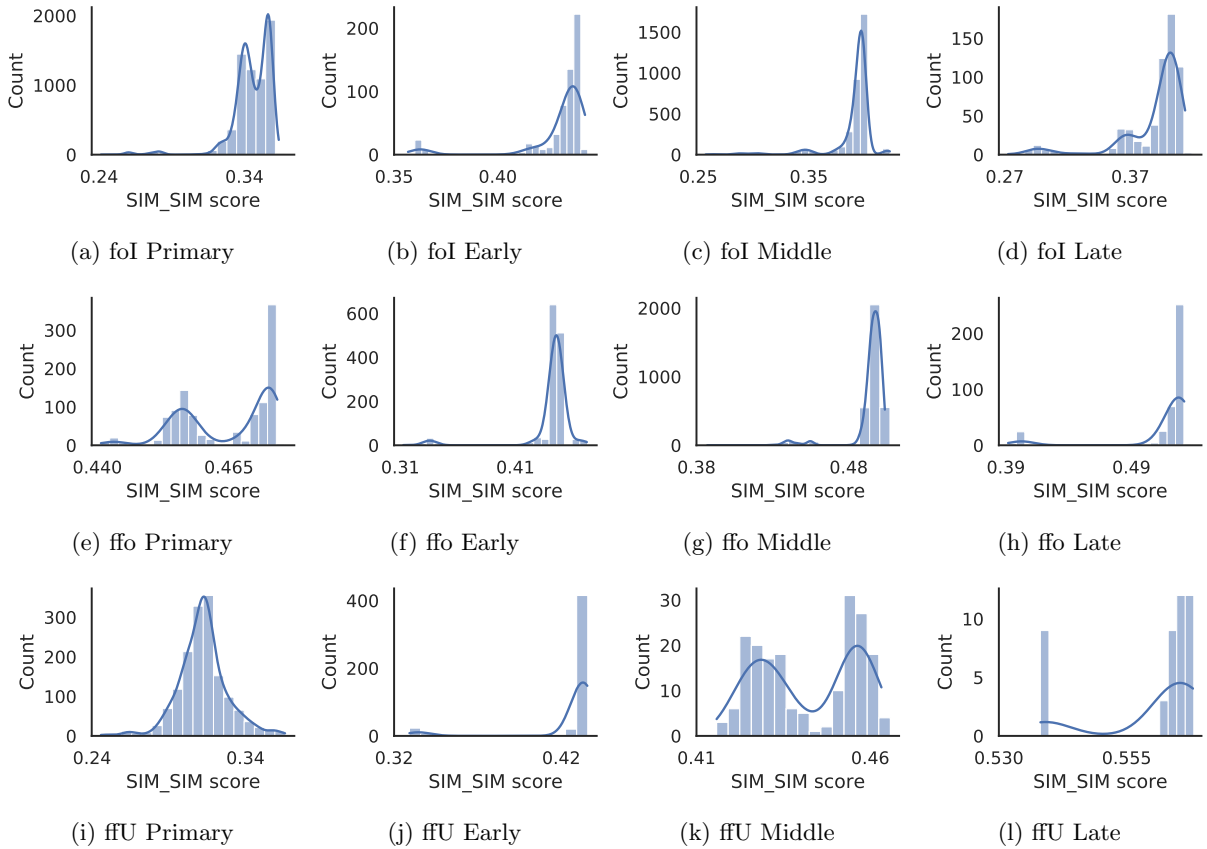


**Figure 14:** kernel density estimation (KDE) plot for  $s_{tgt}^{++}$  prediction with 20 most energetic parts in three different load-cases full front overload (ffo), front oblique overlap (foI), and front small overlap (ffU) in four development stages, primary, early, middle and late that reflects the sequence of the stage, for more information look in Section 3 of [17]. The simulations with less than 0.2 similarities, and outliers, are removed. ( $\Delta t$  [ms],  $IE_{max}$  [kNmm]).

range on the horizontal axis refers to the predicted similarity score, whereas the vertical axis reflects the number of simulation pairs for each value. These KDE plots highlight the differences between each batch, e.g., the score range and the number of peaks. Here, 0.2 seems low for some batches to disregard the outliers, e.g., Figure 14a and 14c. Nonetheless, SimRankTarget++ low computational cost, less than a second, allows users to run the computation interactively with different filtering.

In particular cases, the scores spread is small between simulations, figures 14e and 14l. The narrow range can highlight limited exploration of the designs. Moreover, the singular high density of similarity prediction is related to the number of parts included in the similarity calculation, figures

14c and 14h. Like in the illustrative example, a fully-connected bipartite graph has tighter prediction scores, and the effect of the weights is not as strong as the structure. For example, in a group of FE simulations, a fully bipartite graph means all 20 most energetic parts are the same for all the FE simulations; however, there is a difference between them due to the difference in energy distribution. One approach to extend the deviation of the link prediction score is to include fewer parts to avoid having a fully bipartite graph.

Further, we focus on the similarity predictions for the foI load-case in the primary development stage when considering the 20 most energetic parts, Figure 15. The total number of simulations is 115; consequently, the number of similarities pairs is 6555. A noticeable outcome is that the

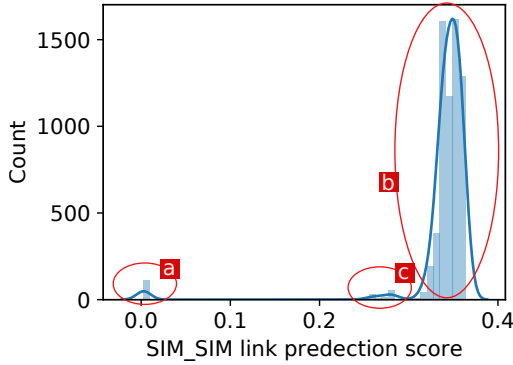


**Figure 15:**  $s_{trgt}^{++}$  link prediction histogram and estimated density for the foI load-case in the primary stage, CEVT data. (a), (b), and (c) highlights the three cluster of similarity distributions.

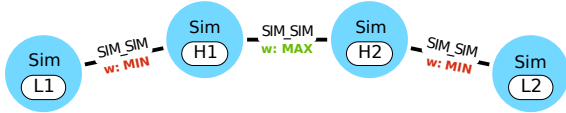


**Figure 16:** H-LL simulation schema selected for each load-case in a development stage based on similarity prediction score.

density of similarity prediction shapes clusters of simulations. In this way, density clustering detects the groups of simulations with similar scores of similarities. Figure 15 has three clusters at (a), (b), and (c), where (a) includes mainly the outliers.

Furthermore, we claim that the cluster with the lowest prediction values includes simulations that reflect outliers, which can be used for anomaly detection. For the considered foI load-case during the primary stage, we manually identified and labeled simulation runs with early termination due to errors or unrealistic high internal energy, respectively. Afterward, we evaluated the similarity score with and without these simulations. We observed that the low-range similarity cluster, i.e., zone (a) in Figure 15, is removed from the density plot when excluding the outlier simulations. The corresponding similarity distribution is plotted in Figure 14a.

## 7.5.2 H-LL simulations

We propose to compare the energy features [17] of several simulations to verify the similarity distances in detail. For that, we select what we call H-LL edges, where H is the edge with the highest similarity, that is the nodes  $H_1$  and  $H_2$ , connected by edge H, are the most similar pair of simulations. The edge is according to the maximum predicted score of  $\bigcirc - \text{SIM\_SIM} - \bigcirc$ . In a second step, we select the corresponding least similar simulations, that is both  $H_1-L_1$  and  $H_2-L_2$ , Figure 16. In some cases,  $L_1$  and  $L_2$  may be the same. We call these H-LL simulations, and we further investigate the results with them to assess the reliability of the predicted similarity.

Table 6 shows a summary of link prediction for the foI load-case during the primary stage. First, we consider all the simulations, Table 6a. Each table row shows the predicted similarity of H-LL simulations while increasing the number of parts. For this data set, the graph is disconnected if we consider less than six most energetic parts. An additional observation is the HL similarity drop after including at least 15 parts in the analysis. Accordingly, the 15 most energetic parts will have the highest similarity range, and afterward, the H-LL pairs are stable.

In a further step, we remove the outlier simulations from cluster (a) in Figure 15. We identify the H-LL simulations while increasing the number of parts included in the bipartite graph, Table 6b. Increasing the number of parts keeps the similarities range shrinking constantly. Generally, parts selection for the similarity assessment is a hyperparameter for the user; however, the H-LL similarities support revealing the differences.

Additionally, we consider a plot using the energy features for a couple of H-LL simulations. With the so-called energy scatter plot [17], one compares the energy features of the most energetic parts of the simulations, which enables us to visually assess the similarity of the simulations' parts in energy absorption. We start with the H-LL<sub>1</sub>,  $\textcircled{354} - \textcircled{387} - \textcircled{237}$ , from Table 6a that  $s_{trgt}^{++}$  that predicted simulation  $\textcircled{237}$  as least similar. Figure 17a visualizes the energy features of 20 parts for each of these three simulations. The plot indicates that simulation  $\textcircled{237}$  has enormous energy in one part, and the simulation ended earlier, causing it to differ noticeably in comparison with the other two

No. Parts	H <sub>1</sub>	H <sub>2</sub>	L <sub>1</sub>	L <sub>2</sub>	$H_1H_2$	HL <sub>1</sub>	HL <sub>2</sub>
6	008	018	386	386	0.486	0.295	0.291
10	004	007	090	090	0.438	0.287	0.294
14	353	354	090	090	0.409	0.266	0.253
15	354	387	237	237	0.401	0.002	0.002
16	354	387	237	237	0.388	0.002	0.002
<b>*20</b>	354	387	237	237	0.364	0.003	0.003

\* H-LL<sub>1</sub>, Figure 17a

(a) All simulations, cluster (a), (b), and (c) in Figure 15

No. Parts	H <sub>1</sub>	H <sub>2</sub>	L <sub>1</sub>	L <sub>2</sub>	$H_1H_2$	HL <sub>1</sub>	HL <sub>2</sub>
2	195	197	354	354	0.477	0.113	0.112
4	354	387	197	197	0.455	0.108	0.123
5	135	197	021	021	0.485	0.236	0.237
6	135	190	287	287	0.492	0.304	0.307
8	354	385	028	028	0.468	0.322	0.346
10	354	357	028	017	0.453	0.340	0.358
12	004	007	287	287	0.442	0.369	0.370
<b>***14</b>	004	007	354	354	0.427	0.375	0.376
16	354	387	017	021	0.405	0.344	0.350
<b>**18</b>	004	007	287	287	0.389	0.349	0.349
<b>*20</b>	354	387	017	017	0.377	0.321	0.331

\* H-LL<sub>2</sub>, Figure 17b\*\*\* H-LL<sub>4</sub>, Figure 17d\*\* H-LL<sub>3</sub>, Figure 17c

(b) Excluding outliers, cluster (b), and (c) in Figure 15

**Table 6:** The H-LL simulations id and their similarities,  $s_{trgt}^{++}$   $C = 0.95$ , prediction score with varying parts included in the bipartite graph, including all the foI load-case simulations in the primary stage, CEVT data.

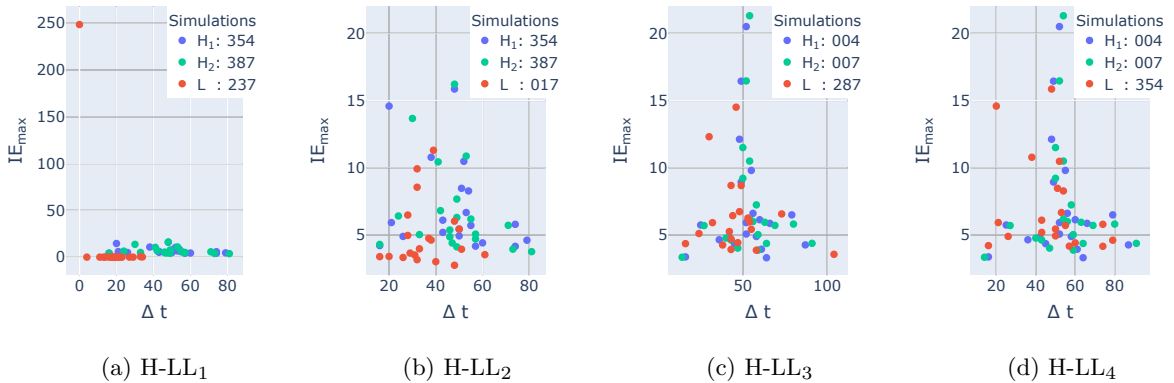


**Figure 17:** Analysis of  $s_{trgt}^{++}$  prediction, energy features for 20 most energetic parts in H-LL simulations for primary development stage and FoI load-case. In all the plots blue-green markers refer to high similarity pairs of simulations and red is the low similarity to them. ( $\Delta t$  [ms],  $IE_{max}$  [kNmm]).

simulations. We expected the least similar simulation to be an outlier, cluster (a) in Figure 15, and this comparison confirms it.

Next, we investigate H-LL simulations from Table 6b excluding the outlier simulations. Here we expect to find the clusters (b) and (c) in the KDE plot, Figure 15. An initial remark from comparing Table 6a and 6b is that the minimum number of required parts in the dataset that avoids having a disconnected graph decreases from six to two, comparing Table 6a and 6b respectively. This drop is an additional cross-check for verifying the filtering of the outliers. Besides, it emphasizes that filtered simulations have the two most energetic parts in common, but there is a flip in its order that we can not decrease it to one part and still have a connected graph. Consequently, there is a bifurcation in the simulations' behavior.

In Table 6b, increasing the number of parts does not settle in one H-LL simulations group, whereas in Table 6a occurs after 15 parts. However, in Table 6b, a trend is observed in H-LL simulations. These groups are marked in Table 6b as H-LL<sub>2</sub>, H-LL<sub>3</sub>, H-LL<sub>4</sub> that includes simulations  $\textcircled{354}-\textcircled{387}-\textcircled{17}$ ,  $\textcircled{4}-\textcircled{7}-\textcircled{287}$ , and  $\textcircled{4}-\textcircled{7}-\textcircled{354}$  respectively. The first and second sets H-LL<sub>2</sub> and H-LL<sub>3</sub> do not overlap in simulations; however, H-LL<sub>4</sub> contains HH simulations of H-LL<sub>2</sub> and H-LL<sub>3</sub>. This observation underlines that two behavior trends are dominant and have a detectable distance from each other.

We look into the energy features scatterplots of these simulations to verify our assumptions. Figures 17b, 17c, and 17d plot energy scatterplots of these simulations for H-LL<sub>2</sub>, H-LL<sub>3</sub>, and H-LL<sub>4</sub> respectively. In Figures 17b and 17c, we see that parts of HH simulations are nearby (blue and green markers), whereas L simulation points are further away (red marker). Furthermore, Figure 17d proves the distance between HH of H-LL<sub>2</sub> and H-LL<sub>3</sub>. Here we can see that the difference is not as noticeable as H-LL<sub>2</sub> and H-LL<sub>3</sub>; parts with lower energy become dominant in similarity prediction if we increase the number of parts.

### 7.5.3 Summary

We used the KDE and H-LL with varying numbers of parts as representations for verifying the similarity scores in the industrial application. For

the practical CAE process, we aim for a discovery platform where the user can actively select the input simulations from KDE distribution and validate that cluster using the H-LL simulations. For now, the novelty of predicting the similarity of simulations and the lack of labeled data requires these types of visualization to assess the similarity results. These visualizations can facilitate the integration of the method into the CAE workflow, which enables the collection of feedback from engineers. The integration of these methods into CAE processes is a critical requirement to enable future improvements using graph analytics.

## 8 Conclusion and outlook

Today, the searchability of the web is an obvious benefit for everyone. However, enhanced searchability still needs to be realized in the CAE domain, where its advantages need to be demonstrated to the engineers. For example, it enables multi-disciplinary collaboration by easing the finding of data within the team and across the company, which increases efficient problem-solving. Moreover, it allows different interconnecting solutions for the same problem and highlights unexplored solutions.

In the context of crash simulation searchability, we focused on predicting the similarity of simulations and a corresponding ranking. Regardless, enhanced searchability will also bring benefit to other CAE domains and other semantics of a domain, e.g., design features, cause and effect analyses, modeling techniques, discipline requirements, and project decisions.

Our graph modeling results in a heterogeneous graph and we need to consider unsupervised learning. To be able to use SimRank-style methods, the only method we found suitable in our scenario, we extracted a bipartite-weighted graph. Additionally, we introduced an alternative weight normalization for SimRank++. The proposed normalization is based on target nodes instead of source nodes. We could show that this works better for our addressed application of predicting the similarity of crash simulations and the corresponding ranking of simulations, shown on a constructed illustrative example with labels.



Additionally, we compared similarity predictions using part-based and component-based approaches. Here we introduced an automatic approach to group the parts and combine the features. While the overall outcome for part-based and component-based similarity is close, the component-based similarity provides a more stable prediction, whereas the part-based similarity is a more sensitive technique. Consequently, we recommend component-based similarity in partial comparison of simulations and part-based for complete model comparison.

On industrial data, we could show that our methods scale up to real data scenarios. Overall, we could verify the simulation similarity prediction, while the data representations showed promise for outlier detection and clustering of simulations based on similarity score distribution.

To further extend the graph-based search capability for the CAE domain we intend extensions of the graph model. For the case of crash simulations, one can consider quantifying the input designs and including different outputs of the simulations. Design features support further link prediction tasks such as the similarity of the FE-models' inputs or cause-effect relations that interconnect the input designs and output features. However, including more simulation outcomes will also require a feature embedding to combine the features or aim for a SimRank formulation with multi-edge weights.

Furthermore, extending applications of graph analytics methods for domain-specific demands will assist cross-domain solutions. Including the multi-discipline requirements as the search object will support ranking the cross-discipline solutions. Another step to enhance searchability is to improve the data labeling to leverage result assessment. Enhanced graph models with larger numbers of simulations stored would also allow applying graph neural networks in this domain.

One approach for improving data labeling is the integration of the current method in companies as a dynamic report platform to collect feedback from engineers, e.g., CAEWebVis<sup>11</sup> introduced in [17]. Only with feedback on the predicted similarities from engineers can one envision a transferring of the unlabeled CAE data to

labeled data. Such labeling will open up new possibilities to empower further ML solutions, e.g., graph neural networks. To allow further investigation of graph analytics for the CAE process, we release our illustrative example, the databases and the source code with a user tutorial<sup>12</sup>.

## 9 Declarations

**Competing interests** The authors have no competing interests, as defined by Springer, or other interests that might be perceived to influence the results and discussion reported in this paper. This work was partly funded by the German Federal Ministry for Education and Research (BMBF) within the project ViPrIA.

## References

- [1] Ackermann S, Gaul L, Hanss M, et al (2008) Principal Component Analysis for Detection of Globally Important Input Parameters in Nonlinear Finite Element Analysis. In: Weimar Optimization and Stochastic Days 5.0
- [2] Antonellis I, Garcia-Molina H, Chang CC (2007) Simrank++: Query rewriting through link analysis of the click graph. In: Proceedings of the 17th international conference on World Wide Web, pp 1177–1178
- [3] Berkhin P (2005) A survey on PageRank computing. *Internet Mathematics* 2(1):73–120
- [4] Center for Collision Safety and Analysis (2015) Toyota Yaris finite element model validation detail mesh. URL <https://www.ccsa.gmu.edu/models/2009-toyota-yaris/>
- [5] Du X, Zhu F (2018) A new data-driven design methodology for mechanical systems with high dimensional design variables. *Advances in Engineering Software* 117:18–28. doi:10.1016/j.advengsoft.2017.12.006
- [6] Du X, Zhu F (2019) A novel principal components analysis (PCA) method

---

<sup>11</sup> Accessible at [CAEWebVis.scai.fraunhofer.de/](http://CAEWebVis.scai.fraunhofer.de/).

<sup>12</sup> [github.com/Fraunhofer-SCAI/GAE-vehicle-safety](https://github.com/Fraunhofer-SCAI/GAE-vehicle-safety).

for energy absorbing structural design enhanced by data mining. *Advances in Engineering Software* 127:17–27. doi:[10.1016/j.advengsoft.2018.10.005](https://doi.org/10.1016/j.advengsoft.2018.10.005)

- [7] Du Bois P, Chou CC, Fileta BB, et al (2004) Vehicle crashworthiness and occupant protection. *Am Iron Stell Inst* pp 27–280, 304–330
- [8] Garcke J, Pathare M, Prabakaran N (2017) ModelCompare. In: *Scientific Computing and Algorithms in Industrial Simulations*. Springer, p 199–205
- [9] Garcke J, Iza-Teran R, Pathare M, et al (2022) Identifying similarities and exceptions in deformations and mesh functions. In: *SIMVEC, Baden-Baden November 2022*
- [10] Iza-Teran R, Garcke J (2019) A geometrical method for low-dimensional representations of simulations. *SIAM-ASA Journal on Uncertainty Quantification* 7(2):472–496. doi:[10.1137/17M1154205](https://doi.org/10.1137/17M1154205)
- [11] Jeh G, Widom J (2002) SimRank: a measure of structural-context similarity. In: *Proceedings of the eighth ACM SIGKDD international conference on Knowledge discovery and data mining*, pp 538–543
- [12] Kracker D, Dhanasekaran RK, Schumacher A, et al (2022) Method for automated detection of outliers in crash simulations. *International Journal of Crashworthiness* pp 1–12
- [13] Kumar A, Singh SS, Singh K, et al (2020) Link prediction techniques, applications, and performance: A survey. *Physica A: Statistical Mechanics and its Applications* 553:124,289
- [14] Lee JA, Verleysen M (2007) *Nonlinear Dimensionality Reduction*. Springer
- [15] Mei L, Thole CA (2008) Data analysis for parallel car-crash simulation results and model optimization. *Simul Model Pract Theory* 16(3):329–337. doi:[10.1016/j.simpat.2007.11.018](https://doi.org/10.1016/j.simpat.2007.11.018)
- [16] Pakiman A, Garcke J (2022) Graph modeling in computer assisted automotive development. *2022 IEEE International Conference on Knowledge Graph (ICKG) ArXiv preprint arXiv:2209.14910*
- [17] Pakiman A, Garcke J, Schumacher A (2022) Knowledge discovery assistants for crash simulations with graph algorithms and energy absorption features. *Applied Intelligence* Accepted
- [18] Patel A, Jain S (2021) Present and future of semantic web technologies: a research statement. *International Journal of Computers and Applications* 43(5):413–422
- [19] Schembera B, Durán JM (2020) Dark data as the new challenge for big data science and the introduction of the scientific data officer. *Philosophy & Technology* 33(1):93–115
- [20] Schwanitz P (2022) Towards AI based recommendations for design improvement (AI-B-REDI), presentation at *SIMVEC, Baden-Baden November 2022*
- [21] Schwanitz P, Greve L, Moldering F, et al (2022) Towards AI based recommendations for design improvement (AI-B-REDI). In: *SIMVEC, Baden-Baden November 2022*
- [22] Wang H, Wei Z, Liu Y, et al (2021) ExactSim: benchmarking single-source SimRank algorithms with high-precision ground truths. *The VLDB Journal* 30(6):989–1015
- [23] Wang Y, Wang Z, Zhao Z, et al (2020) Effective similarity search on heterogeneous networks: A meta-path free approach. *IEEE Transactions on Knowledge and Data Engineering* 34:3225–3240